Proceedings of 2004 Korea-Japan Joint Seminar
on Particle Image Velocimetry
POSTECH, Korea, Dec. 9 - 10

4-D PTV

Deog Hee Doh* and Koji OKAMOTO**

*Flow Visualization Laboratory, Korea Maritime Univ.,
Dongsam-dong, Youngdo-ku, Busan, 606-079, Korea
doh@mail.hhu.ac.kr
**Nuclear Engineering Research Laboratory, The University of Tokyo,
Tokai-mura, Ibaraki, 319-1188, Japan
okamoto@utnl.jp

Abstract: A 4D-PTV system was constructed. The measurement system consists of three high-speed high-definition cameras(1k x 1k, 2000fps), Nd-Yag laser(2000Hz) and a host computer. The GA-3D-PTV algorithm was used for completing the measurement system. The 4D-PTV is capable of probing the spatial distribution of velocity vectors of the flow field overcoming the temporal resolution of the characteristic turbulence length scales of the measured flow fields. A horizontal impinged jet flow (H/D=7) was measured. The Reynolds number is about 33,000. Spatial temporal evolution of the jet flow was examined and physical properties such as spatial distributions of vorticity and turbulent kinetic energy were obtained with the constructed.

Keywords: 4D-PTV, GA-3D-PTV algorithm, Impinged Jet, Vortex Ring

1. Introduction

For heat transfer enhancements, impinged jets are widely used because there are high heat and mass transfer coefficients region near its stagnation are. For this reason, they are found in wide application in a variety of industries such as, cooling turbine-blade and the surface of combustor and a semiconductor in the electronic equipment.

Submerged impinged jets have received substantially more attention in the literature than have impinging free liquid jets. The stagnation point velocity gradient had been shown by many pervious analytical and experimental investigations to be an important parameter in stagnation heat transfer (Sibulkin, 1952; Burmeister, 1983). The magnitude of the heat transfer coefficient found to be influenced by the stagnation line velocity gradient so that a narrower jet provided higher heat transfer coefficients. Several related factors, including the jet exit velocity profile, and stagnation region radial velocity gradient have been proposed to be of importance in governing the heat transfer under an impinged jet (Vader et al., 1991; Stevens and Webb, 1991). All of these factors are known to influence the heat transfer on the surface of the impinging plate. Olsson and Turkdongan (1966) investigated experimentally the radial flow field of an impinged liquid jet with pointwise measurement results. Gardon et al. (1965) discovered how the turbulent flow can effect heat transfer when free jet was impinged on the surface of a plate. Kataoka et al.(1986) discovered through pointwise measurements that period of vortex could change the effect of heat transfer at the impinging plate after observing a large period vortex on the round nozzle jet. Most of the results obtained by previous researches were based on a pointwise measurement technique such as, Hot wire and LDV, or numerical simulations. No matter how the numerical results are accurate, the results should be proved with the results obtained through an experiment because the flow

fields are too complicate to be analyzed accurately. In order to attain accurate analysis on the impinged jet, it is necessary to know vortical structures of the jet. There have been some efforts to study the influence of the flow structures of an impinged jet on heat transfer. Faggiani and Grassi (1990a, 1990b) studied the influences of the local and average heat transfer characteristics by studying the influence of flow structure on transport with the results on large-scaled flow structures. Bae et al. (2001) investigated the influence of the impinged angles with PIV. They could get their results with a fieldwise measurement, PIV (Particle Image Velocimetry) and LCM (Liquid Crystal Method). However, the results proposed by them were based on 2-dimensional PIV technique or 2-dimensional-field measurement technique. To make a complete analysis on the influences of the flow structures of the jet, 3-dimensinal measurements are even more necessary. Nishino et al. (1996) carried out 3D-PTV measurement on the impinged jet and provided statistics of the turbulent properties near the stagnation region. Since the number of instantaneous velocity vectors obtained was not so many, the structural analysis on the impinged jet couldn't be made. Recently, Nishino and Takahashi (2003) introduced a dynamic PIV system for the jet experiments to overcome the limits of the time resolution of the conventional PIV measurement system for the frequency of the flow field and tried to find out structures of the jet with high resolution using high-definition camera (1K x 1K). In order to attain more accurate study into the influences of the vortical structures of the impinged jet on the heat transfer of heated plates, it is necessary that the number of instantaneous three-dimensional velocity vectors should be enough. Mass et al. (1993) could get more than 1000 instantaneous three-dimensional velocity vectors for three-dimensional channel flow with a three-camera arrangement. However, the flow field was restricted to the boundary region of a channel flow. In the mean while, Doh et al. (2002) obtained more than 98% of correct vectors from initial velocity vectors for a forced vortex flow field by introducing a genetic algorithm (GA) to the conventional 3D-PTV system. They took a consideration onto the disappearing particles' pairs between two image frames and reused those particles pairs for GA calculation to enhance the recovery ratio of correct vectors. They obtained more than 3000 instantaneous three-dimensional velocity vectors for the wake of a sphere with low resolution cameras (0.5K x 0.5K)(2004). The aim of this study is to construct a system called 4D-PTV system that overcomes the limits of the temporal and spatial resolutions of the conventional PIV system by revising their algorithm of the 3D-GA-PTV (2002, 2004) and by introducing high-definition-high-speed cameras and a high-speed pulsed laser system to the conventional 3D-PTV hardware system, and to construct the database of the impinged jet.

2. Measurement System

2.1 Experimental Setup and Procedures

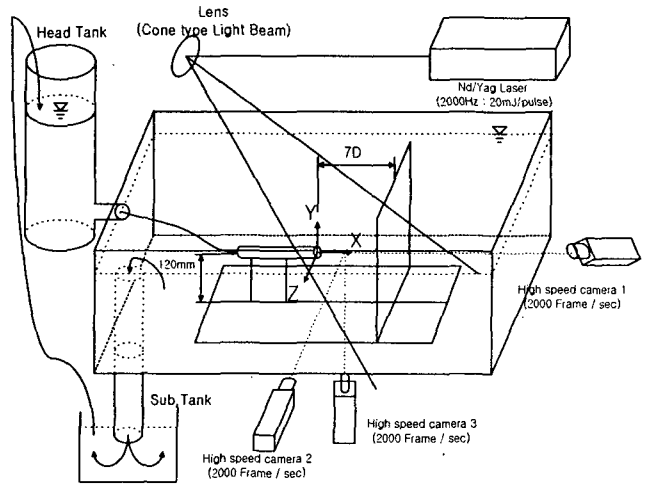

Fig. 1 4D-PTV system for the impinged jet flow.

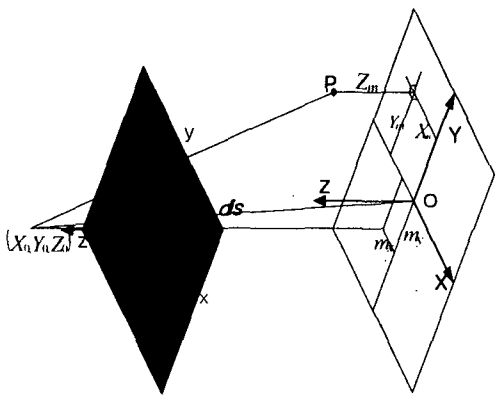

Fig. 2 Relations of camera parameters on the absolute and the photographical coordinates.

Fig. 1 shows the experimental setup. The Reynolds number is about 33,000 with the nozzle diameter D=20mm. The distance between the flat plate and the nozzle is H/D=7. Three Photron Fast CAM APX(Max) cameras and Coherent Corona Laser (10mJ, 2000Hz) were used to overcome temporal and spatial resolution of the conventional 3D-PTV system. The image resolution of the camera is 1024 x 1024 pixel with 2000 fps. Using the camera, the high-temporal and spatial resolution images could be captured. All hardware components of the system were synchronized for simultaneous image capturing.

A multi-sectioned calculation algorithm used for the calculation of the GA-Based 3D-PTV algorithm (Doh et al., 2002, 2004) in order to save the calculation time. The size of the measurement region is 90mm x 90mm x 90mm. The origin of the absolute coordinate (X=0, Y=0, Z=0) for the impinging jet was defined at the center position between the nozzle and the plate along the centerline of the jet. For the measurement of 3D-PTV, camera calibration is carried out using a calibrator on which 42 landmarks are installed. Before using it as the landmarks for the camera calibration, the three-dimensional positions of these landmarks were measured by an optical system (BLN-C797) which has a precision of ±0.001mm. The calibrator is set into the measurement volume for the calibration. The apertures of the three cameras have been adjusted to focusing on the whole landmarks' images in order not to be affected largely by the influence of the blurred particles' images due to the limits of the depth of focus. After completing the calibration for the three cameras and the construction of the flow field, tracer particles (diameter=100 ㎛, specific gravity=1.02) were put into the flow field and visualization was carried out the laser light. The volume light illumination direction was set to produce a fore-scattering for all three cameras in order to make the particles' images to be seen more clear as seen in the Fig. 1. The images captured by the three cameras were transferred to the host computer in which the centroids of the particles were calculated. In this study, the three-dimensional vectors were obtained by the calculation of the GA-Based 3D-PTV algorithm (Doh et al., 2002) using the particles' centroids.

2.2 4D-PTV System

To get the three-dimensional velocity vectors, camera parameters such as the exterior (the position and the orientations of the camera) and the interior parameters (the focal length, deviations of the principal point and the distortion coefficients of the camera lens) were obtained in advance. Next, three-dimensional position of each particle was calculated. Finally, three-dimensional velocity vectors were calculated.

In this study, 10 parameters (6 exterior parameters: $dis, \alpha, \beta, \gamma, m_x, m_y$, 4 interior parameters: c_x, c_y, k_1, k_2) were obtained. (α, β, γ) represents the tilting angles of the axes of the photographic coordinates against the absolute axes. Fig. 2 shows a coordinate relation when the photographical axes had been set to parallel with the absolute coordinate by tilting with the angles (α, β, γ). (X, Y, Z) represents the absolute coordinate, and (x, y, z) the photographical coordinate of the objective point. The notation *dis* means the distance between the origin O(0, 0, 0) and the principal point (X_0, Y_0, Z_0) of the camera.

$$x = c_x \frac{Y_m - m_x}{\sqrt{dis^2 - m_x^2 - m_y^2} - Z_m} + \Delta x \quad , \quad y = c_y \frac{Y_m - m_y}{\sqrt{dis^2 - m_x^2 - m_y^2} - Z_m} + \Delta y \tag{1}$$

$$\Delta x = (x/r) \times \left(k_1 r^2 + k_2 r^4\right), \quad \Delta y = (x/r) \times \left(k_1 r^2 + k_2 r^4\right), \quad r = \sqrt{x^2 + y^2} \tag{2}$$

The coordinate (X_m, Y_m, Z_m) represents the position of the point P when the camera coordinate is rotated with the tilting angles to make the collinear set in one line as shown in Fig. 3. The m_x, m_y means the point at which the normal vector from the origin O(Xo, Yo, Zo) of the camera coordinate meets with the X-Y plane. The collinear equation for every point between the two coordinates is expressed as Eq. (1). c_x and c_y are the focal distances for x and y components of the coordinate. Δx and Δy are the lens distortions as expressed as Eq. (2). The Eq. (1) can be converted to the following Eq. (3).

$$F = c_X \frac{X_m - m_X}{\sqrt{dis^2 - m_X^2 - m_Y^2} - Z_m} - (x - \Delta x) = 0, \quad G = c_Y \frac{X_m - m_X}{\sqrt{dis^2 - m_X^2 - m_Y^2} - Z_m} - (y - \Delta y) = 0 \quad (3)$$

Since this equation is a strong non-linear, an improved Gauss-Newton calculation method [4] was adopted to obtain all necessary parameters using the above two equations in Eq. (3). Once all camera parameters are obtained, the relations between the photographic coordinate and the absolute coordinate of the targets' image or the particles' image can be expressed as the following Eq. (4).

$$\begin{bmatrix} X \\ Y \\ Z \end{bmatrix} = \mathrm{M}_M^{-1} \begin{bmatrix} X_m \\ Y_m \\ Z_m \end{bmatrix} = \mathrm{B} \begin{bmatrix} X_m \\ Y_m \\ Z_m \end{bmatrix} \quad (4)$$

Here, M_M is the matrix for the rotational transformation and B is its reverse matrix. (X_m, Y_m, Z_m) is expressed in the form of Eq. (5).

$$\mathrm{X}_m = \frac{x - \Delta x}{c_x} t + m_X, \quad \mathrm{Y}_m = \frac{y - \Delta y}{c_y} t + m_y, \quad \mathrm{Z}_m = \mathrm{d} - \mathrm{t}, \quad \mathrm{d} = \sqrt{dis^2 - m_X^2 - m_y^2} \quad (5)$$

If the center of the camera is set to a vector (Xo, Yo, Zo), the collinear equation for one target (or particle) can be expressed as P(X, Y, Z) = (a_1 t + Xo, a_1 t + Yo, a_3 t + Zo). The cross-sectional points constructed from the following two collinear equations for the two cameras are defined as the three-dimensional positions in the absolute coordinate.

$$\mathrm{A(X, Y, Z)} = \mathrm{A}(a_{11} t + b_{11}, a_{12} t + b_{12}, a_{13} t + b_{13})$$
$$\mathrm{B(X, Y, Z)} = \mathrm{B}(a_{21} s + b_{21}, a_{22} s + b_{22}, a_{23} s + b_{23}) \quad (6)$$

Here, t and s are obtained by the least square method (LSM). Since the cross-sectional points do not always intersect on one point, the below Eq. (7) was used for the definition of the last three-dimensional position of the targets (or the particles), which implies the center of the shortest distance between the two collinear equations expressed as Eq. (6).

$$\begin{bmatrix} X_P \\ Y_P \\ Z_P \end{bmatrix} = \frac{1}{2} \left\{ \begin{bmatrix} X_A \\ Y_A \\ Z_A \end{bmatrix} + \begin{bmatrix} X_B \\ Y_B \\ Z_B \end{bmatrix} \right\} \quad (7)$$

Here, X_A, Y_A and Z_A represent the absolute coordinates for camera A defined by Eq. (6). X_B, Y_B and Z_B are for camera B. In order to calculate the three-dimensional positions of particles, corresponding pairs the centroids of particles of the two sets of camera images should be discovered among many other particles. A genetic algorithm based 3D-PTV algorithm has been adopted in order to find the true corresponding pairs. Detailed calculation process for finding the pairs can be referred to the study of Doh et al. (2002). Since the image data are large, a multi-section calculation method was introduced to save the calculation time in which the measured volume was divided into four districts. In this case, the 3D-GA-PTV calculation was carried out by using each image set corresponding to each district.

3. Measurement Results

3.1 Transient Velocity Tracking

Fig. 3 shows one of the instantaneous raw images captured by the camera 2 located as in Fig. 1. Fig.

4 shows the instantaneous three-dimensional velocity vectors. The number of the instantaneous vectors obtained in one processing was about 10,000. Among these erroneous vectors are eliminated using the Tompson's Tau Method (ANSI/ASME, 1983) in which the correct vectors are only selected in a small volume that corresponds to the size of a virtual probe sensor. The number of vectors judged as correct ranged between 5000 and 6000. Fig. 5 shows the ensemble grid vectors which were obtained from the correct vectors after eliminating the erroneous vectors using 2000 image frames. Fig. 6 shows instantaneous vorticity distribution. The distribution represents the vorticity ($\omega = (\omega_x^2 + \omega_y^2 + \omega_z^2)^{1/2}$)at three YZ planes at x/D = 2.3, 3.5 and 5.1. It can be said that there exist ring vortexes along the axis of the jet, which can be explained by vorticity distribution on XY center plane as shown in Fig. 6.

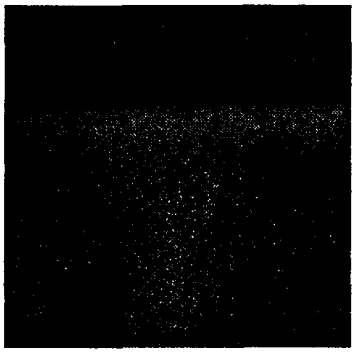

Fig. 3 Raw image of camera 2.

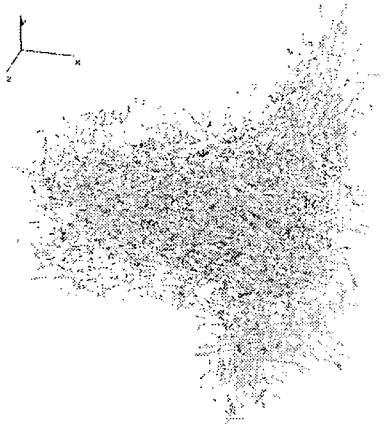

Fig. 4 Instantaneous vectors with error vectors.

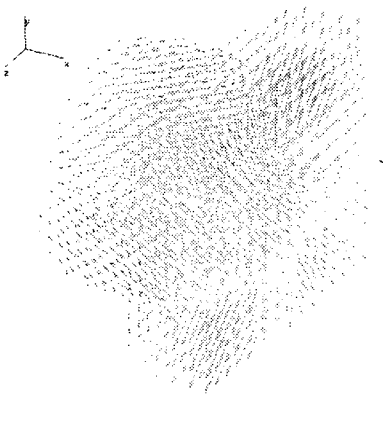

Fig. 5 Ensemble averaged grid vectors.

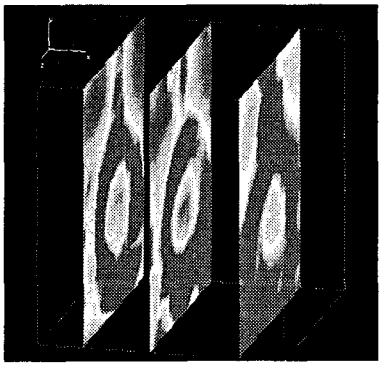

Fig. 6 Instantaneous vorticity distribution on YZ planes at x/D=2.3, 3,5 and 5.1.

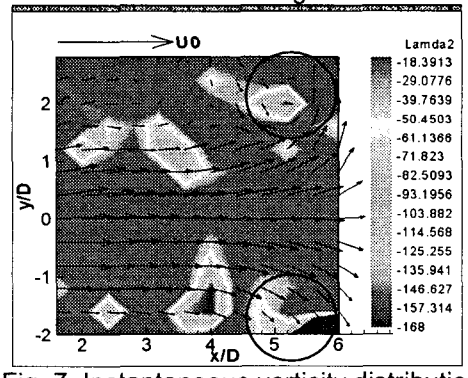

Fig. 7 Instantaneous vorticity distribution on XY center plane.

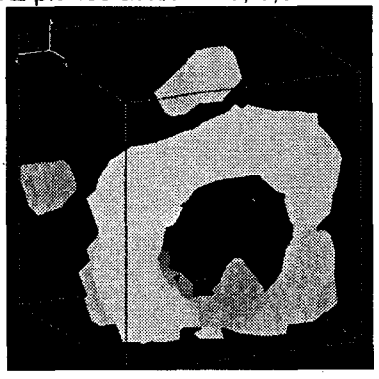

Fig. 8 Vortex loop obtained by 4D-PTV.

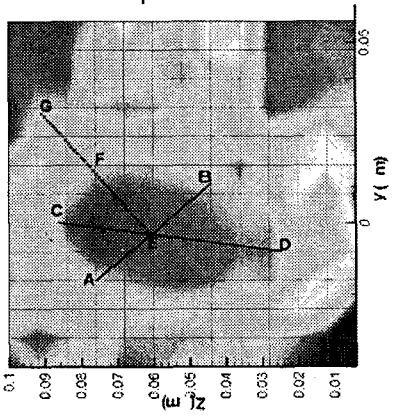

Fig. 9 Topology of the vortex loop.

According to the report made by Kataoka et al.(1986), it is known that the periodical vortex series can change the effect of heat transfer at the impinging plate after observing a large period vortex on the round nozzle jet. This fact can be explained by the series of vortical structures as seen in Fig. 6 and Fig. 7. In order to make out characteristic structures of the vortices, an eigenvalue analysis suggested by Jeong and Hussain (called as λ_2 method, 1995) was introduced. The instantaneous three-dimensional velocity vectors on grids obtained by the constructed 3D-PTV system can be expressed into velocity gradient tensor ($\nabla\vec{u} = u_{i,j}$, vorticity tensor) and the characteristic equation can be approximated with the Taylor series Expansion expressed as the below Eq. (8).

$$\sigma^3 - P\sigma^2 + Q\sigma - R = 0, \quad P = u_{i,j}, \quad Q = \frac{1}{2}\left(u_{i,j}^2 - u_{i,j}u_{j,i}\right), \quad R = Det\left(u_{i,j}\right) \tag{8}$$

The vortex core exist when the eigenvalue of this characteristic equation has complex values, which implies that the vortex core can be found when the sign of the discriminant equation expressed as the below Eq. (9) is positive.

$$\Delta = \left(\frac{1}{3}Q\right)^3 + \left(\frac{1}{2}Q\right)^3 > 0 \tag{9}$$

Since the impinged jet flow field is very complex, the obtained values showed positive values almost over the measured volume, i.e., eigenvalues were complex values. This implies that the flow field is filled with complex vortices. In order to figure out more representative vortices from this flow field, the characteristic equation was transformed to a new tensor A_{ij} consisting of symmetric (S_{ij}) and asymmetric (R_{ij}) tensors defined as Eq. (10) (i.e., $A_{i,j} = S_{i,j}S_{i,j} + R_{i,j}R_{i,j}$) and the real roots of

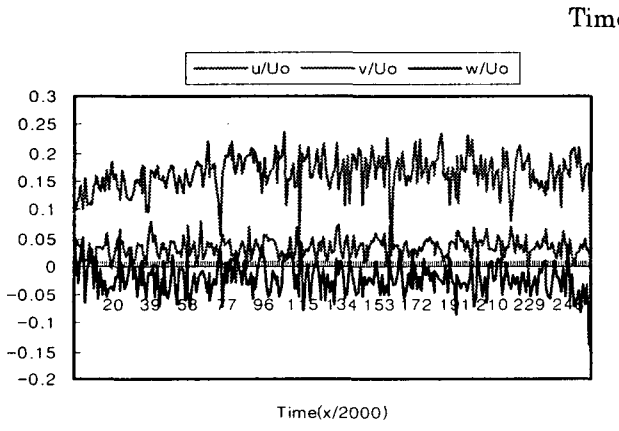

Fig. 10 Temporal evolution of velocity components. (at x/D=5.9, y/D= 1.4, z/D= -0.1, step= 0.5 msec)

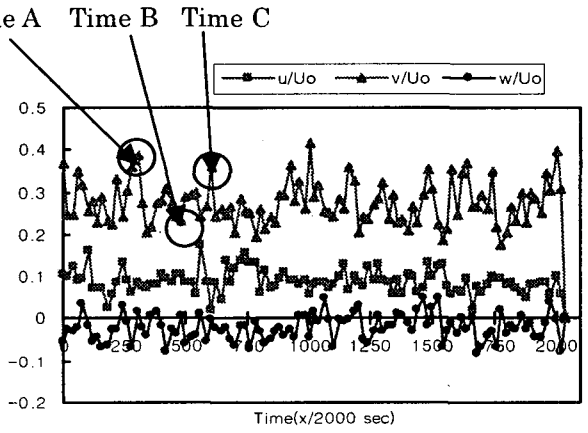

Fig. 11 Temporal evolution of velocity components. (at x/D= 5.8, y/D= 2.4, z/D= 0, step= 10 msec)

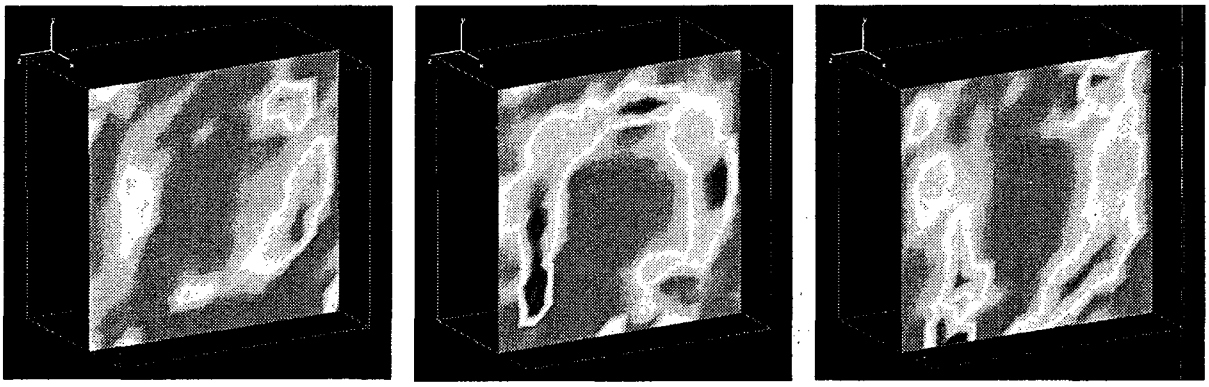

(a) at Time A = 251/2000 sec (b) at Time B = 481/2000 sec (c) at Time C = 681/2000 sec

Fig. 12 Temporal changes of the vortex ring structures at the times figured out on Fig. 11.

the discriminant equation of the characteristic equation for the new tensor was evaluated and sorted stepwise to find characteristic vortical structures.

$$S_{i,j} = \frac{1}{2}\left(u_{i,j} + u_{j,i}\right), \quad R_{i,j} = \frac{1}{2}\left(u_{i,j} - u_{j,i}\right) \tag{10}$$

Fig. 8 shows the vortical structure when the eigenvalue of the new characteristic equation shows the second biggest value among the eigenvalues and these values were 5% of the maximum value over the flow field. It can be said that a large vortex loop exists near the impinging plate. Fig. 9 represents the cutoff section of the ring vortex obtained at another instance. It showed that the location of the center of the vortex loop was near 0.9D from the plate. It also showed that the thickness of the vortex loop was about 0.8D (line of FG). The inner diameter of the loop was 1.8D (line of AB). According to the study of Astarita et al. (2001), the minimum and maximum in heat transfer coefficients are seen at r/D=1.3 and r/D=2.2. This implies that the vortex mainly influence the heat transfer. The topological results obtained by the constructed 4D-PTV support well this fact.

Fig. 10 shows the temporal evolution of the results measured for 256 consecutive image frames at x/D= 5.9, y/D= 1.4, z/D= -0.1. The time step is 0.5 msec (=1/2000 frames/sec). It is seen that v/Uo is 0.15 showing periodical peaks with time evolution while u/Uo and w/Uo components show stationary random fluctuation near zero. This explicitly supports the existence of a strong ring vortex in front of the plate. The periodical time difference between conspicuous peaks (peak to peak) of v/Uo component ranged between 25/2000 ~ 40/2000 sec(12.5msec ~ 20msec). It can be said that the time interval corresponds to the passing interval of the ring vortices over the surface of the impinging plate. Considering this time interval, velocity components were sampled with 10msec time interval from the whole 2000 image frames in order to figure out the temporal topology of the ring vortex. Fig. 11 shows the temporal evolution of the velocity sampled at each 10msec at x/D= 5.9, y/D= 2.4, z/D= 0. In a common sense, it can be estimated that the structure of the ring vortex at the Time A and Time C would be similar each other while the structure at the Time B would be a topologically different one. Surprisingly, two conspicuous structures were seen at Time A (=C) and Time B as expected. Fig. 12 show the ring vortex structure obtained by the λ_2 method at the cutoff section. It can be said that the appearance of the two structures with some time interval implies that the vortex ring are "squeezed periodically in horizontal and in vertical" due to the vortex interactions between the smaller vortices embedded in the ring vortex.

4. Conclusion

4D-PTV technique was constructed through an experiment on an impinged jet using non-metric high-speed-high-definition cameras. More than 5000 instantaneous correct vectors were able to be measured by the system.

The ring vortex was clearly reconstructed by the obtained velocity vectors through an eigenvalue analysis. The location of the ring vortex, 0.9D from the plate, was at reasonable positions which were confirmed by previous research results. And the thickness of the ring vortex was about 0.8D. The results showed that the sweeping velocity of the ring vortex over the surface of the impinging plate ranged between 12.5msec and 20msec, which implies that the ring vortex has strong relations with the convection velocity of the ring vortex.

It seems that the ring vortex appears periodically and shows a squeezing motion in horizontal and in vertical with time intervals.

The results obtained in the experiment of the impinged jet implies that the system not only makes possible to obtain the temporal evolution of turbulence properties but also makes possible to capture the instantaneous flow structures.

To use the 4D-PTV system for higher turbulences, the least sampling frequency of the system should be higher than that of the flow fields, which implies the 4D-PTV system should be able to sample faster than the representative physical time scale (ex, Taylor micro scales), particles' Lagrange frequencies.

Complete and direct probing corresponding to DNS of numerical analysis on complex flow fields can be attained when higher-definition cameras are used.

Acknowledgements

This work was carried out as parts of the Brain Korea Project of Ministry of Education of Korea (BK21). And it was partly supported by Korea Research Foundation Grant (KRF-2004-002-D00082). The authors would like to express sincere thanks to Dr. M. Ishikawa of Tokyo Univ. for his helps for the experiments.

References

ANSI/ASME MFC-2M-1983, Measurement Uncertainty for Fluid Flow in Closed Conduits, ASME United Eng. Center, 1983.

Astarita, T., Cardone, G. and Meola, C., Fluid Dynamics in an Impinging Air Jet, Proc. of 4th International Symposium on Particle Image Velocimetry, Göttingen, Germany, Paper No. 1015, 2001.

Bae, S.T., Kim, D.K. and Kim, S.B., An Experimental Study on Flow Characteristics of Impinging Jet, Journal of the Korean Society of Marine Engineers, 25-2 (2001), pp.173-179.

Burmeister, L. C., Convective Heat Transfer, Wiley, New York, 1983.

Doh, D.H., Kim, D.H., Cho, K.R., Cho, Y.B., Saga, T. and Kobayashi, T., Development of GA based 3D-PTV Technique, Journal of Visualization, 5-3 (2002), pp.243-254.

Doh, D.H., Hwang, T.G., Saga, T., 3D-PTV measurements of the wake of a sphere, Measurement Science and Technology, 15-6, pp.1059-1066.

Faggiani, S. and Grassi, W., Impinging Liquid Jets on Heated Surfaces, Proc. of the 9th International Heat Transfer Conference, 1 (1990a), pp.275-285.

Faggiani, S. and Grassi, W., Round Liquid Jet Impingement Heat Transfer: Local Nusselt Numbers in the Region with Non Zero Pressure Gradient, Proc. of the 9th International Heat Transfer Conference, 4 (1990b), pp.197-202.

Gardon, R. and Akfrat, J.C., The Role of Turbulence in Determining the Transfer Characteristics of Impinging Jet. Int. J. Heat Mass Transfer, 8 (1965), pp.1261-1272.

Jeong, J. and Hussain, F., On the Identification of a Vortex, Journal of Fluid Mechanics, 285 (1995), p.69.

Kataoka, K., Mihata, I., Maruo, K., Suguro, M. and Chigusa, T., Quasi Periodic Large Scale Structure Responsible for the Selective Enhancement of Impinging Jet Heat Transfer, Proc. of the 8th Int. Heat Transfer Conf., 3 (1986), pp.1193-1198.

Mass, H.G., Gruen, A. and Papantoniou, D.A., Particle Tracking Velocimetry in Three-dimensional Flows, Part 1 Photogrammetric Determination of Particle Coordinates, Exp. in Fluids, 15 (1993), pp.133-146.

Nishino, K., Samada, M., Kasuya, K. and Torii, K., Turbulence Statistics in the Stagnation Region of an Axisymmetric Impinging Jet Flow, Int. J. Heat and Fluid Flow, 17 (1996), pp.193-201.

Nishino, K. and Takahashi, T., High-speed PIV Applied to a Submerged Circular Impinging Jet, Proc. 5th International Symposium on Particle Image Velocimetry(PIV'03), Busan, Korea, Paper No.3217, 2003.

Olsson, R.G. and Turkdogan, E.T., Radial Spread of a Liquid Stream on a Horizontal Plate, Nature, 211 (1966), pp.813-816.

Sibulkin, M., Heat Transfer near the Forward Stagnation Point of a Body Revolution, Journal of the Aeronautical Sciences, 9 (1952), pp.570-571.

Stevens, J. and Webb, B.W., Local Heat Transfer Coefficients under an Axisymmetric, Single-phase Liquid Jet, ASME, Heat Transfer, 113 (1991), pp. 71-78.

Vader, D.T., Incropera, F.P. and Visskanta, R., Local Convective Heat Transfer from Heat Surface to an Impinging Planar Jet of Water, International Journal of Heat and Mass Transfer, 34-3 (1991), pp.611-623.